Available online at https://link.springer.com/journal/42241
http://www.jhydrodynamics.com
Journal of Hydrodynamics, 2023, 35(2): 314-329
https://doi.org/10.1007/s42241-023-0023-1

Numerical investigation of the effect of wedge-type cavitating-bubble generator on attached unsteady cavitating flows using proper orthogonal decomposition method

Bo-jie Hong[1], Chang-li Hu[1*], Zhi-ying Wang[2], Hao-jie Xing[1]
1. *School of Energy and Power Engineering, Nanjing University of Science and Technology, Nanjing 210094, China*
2. *Key Laboratory for Mechanics in Fluid Solid Coupling Systems, Institute of Mechanics, Chinese Academy of Sciences, Beijing 100190, China*

(Received October 3, 2022, Revised December 30, 2022, Accepted January 7, 2023, Published online May 11, 2023)

Abstract: The objective of this work is to reveal the effect of a passive control method called wedge-type cavitating-bubble generator (WCG) on the cloud cavitation dynamics of National Advisory Committee for Aeronautics (NACA) 66 hydrofoil. The simulations are performed using the Partially-averaged Navier-Stokes (PANS) method coupled with the Zwart cavitation model. The proper orthogonal decomposition (POD) method is applied to extract the dominant flow structures. The results show that the WCG can induce the attached cavity to occur just behind the WCG instead of the hydrofoil leading edge. During the periodical time-evolution process of the unsteady cavity, it is found that the attached cavity with a larger scale around the hydrofoil with WCG has a rougher surface, accompanied with more shedding behaviors of small cavities. This is further illustrated by the POD modes, that is, the mode 1 and modes 2-4 present the large and small cavity vortex structures respectively. Meanwhile, the dominant frequencies of 50 Hz, 47.5 Hz are given by the POD method respectively for the hydrofoils without and with WCG, which is in good agreement with that of FFT analysis. In addition, the correlation distribution of POD modal coefficients shows that the WCG can strengthen the vortex energy as well as the turbulence intensity.

Key words: Cavitating-bubble generator, proper orthogonal decomposition (POD), attached cavity, vortex structures

0. Introduction

Cavitation is a complex phase-change phenomenon, which commonly occurs in marine engineering and hydraulic machinery systems. It is well known that the unsteady cavitation will cause various destructive and undesirable effects, such as erosion, vibration and noise[1]. Therefore, the investigation of controlling cavitation is necessary and promising for engineering applications.

Recently some passive methods, such as changing the wall roughness, installing obstacles on the surface, etc. have been applied to control cavitation, especially restraining the unsteady behaviors. Coutier-Delgosha et al.[2] studied the effect of surface roughness on the cavitation characteristics on a 2-D foil section. The results showed that the roughness weakened the kinetic energy of the re-entrant jet, reduced the cavity length, and suppressed the cavity shedding. Kawanami et al.[3] installed a 2 mm×2 mm rectangular cross-section obstacle at 37% of the foil chord length. They found that the re-entrant jet could not reach the leading edge of the cavity to cut it off, then the formation of cloud cavitation was suppressed. This conclusion can also be obtained from the study of Zhang et al.[4]. Huang et al.[5] reported that the trip bar placed on the surface of projectile could weaken the re-entrant jet and prevent the pressure wave caused by the cavity rupture, so that a stable sheet cavity could be formed between the shoulder of projectile and trip bar. Zhao and Zhao[6] showed that the obstacles placed on the suction surface of the centrifugal pump impeller could cause relatively high pressure on the impeller surface and optimize the flow structure, resulting in the cavitation being suppressed to a certain extent. In addition, Cheng et al.[7-9] investigated the tip-leakage vortex (TLV) cavitation and showed that TLV cavitation can be well controlled by installing the overhanging grooves (OHGs) at the hydrofoil tip.

Among these passive controlling methods of

Project supported by the National Natural Science Foundation of China (Grant No. 52076108).
Biography: Bo-jie Hong (1998-), Male, Master,
E-mail: hbj2915673846@163.com
Corresponding author: Chang-li Hu,
E-mail: changlihu@njust.edu.cn

cavitation, the vortex generator (VG) is a promising technology, which was first applied in the field of aerospace engineering. Using this method, the streamflow vortices can be generated to mix the fluid inside and outside the boundary layer, thus delaying the flow separation and increasing the lift. Lu et al.[10] showed that VGs installed on both sides of the stern could induce the sheet cavity more stable and reduce the surface pressure fluctuation by 1/2 to 1/3. Che et al.[11-12] studied the control effect of micro-vortex generators (MVGs) on the attached cavitation and found that the MVGs played the role of rectification for the flow near wall and fixed the initial position of the cavity. In addition, another derived passive control cavitation device called cavitating-bubble generator (CG) was proposed recently. Kadivar et al.[13-14] studied the influence of cylindrical cavitation generators (CCGs) mounted at different locations on cavitating flow. They found that the CCGs inserted in a proper position could reduce the strength of the re-entrant jets and suppress the instability behavior of the cloud cavitation. This result can also be achieved by installing the hemispherical vortex generators near the cavitation inception location[15]. Moreover, they pointed out that the wedge-type cavitation-bubble generator (WCG) inserted in the turbulent boundary layer could reduce the amplitude of pressure pulsation in the wake region and prevent the formation of cavitation cloud[16-17]. Javadi et al.[18] found that the stable cavitating bubble could be formed behind the WCG if the WCG was located near the cavitation inception on the suction surface of the 2-D hydrofoil. As mentioned above, most of the previous studies mainly focused on the effect of cavitation-bubble generators on suppressing the instability or fluctuation of cloud cavitating flows. Moreover, the WCG was always installed in the separation region or its downstream. However, some previous studies indicated that the laminar separation played a vital role in attached cavitation inception[19-20]. As a result, we attempt to place the WCG upstream the laminar separation bubble to the highest degree of controlling it. Also, the influence of WCG on the inception and turbulence vorticity structures of unsteady attached cavitation will be investigated.

The proper orthogonal decomposition (POD) method has been widely applied to study the cavitating flows in recent years. Danlos et al.[21] used the POD method to decompose the velocity fields of different longitudinal grooved surfaces in the venturi tube. They found that the POD method could identify the cavitation state and the shedding frequency of cloud cavitation. Wang et al.[22] applied the POD method to reveal the effect of ventilated cavitation on vortex shedding. They found that the energy of the first two modes decreased with the increase of the gas entrainment coefficient Q_v, indicating that the strength of the large-scale vortex structure was weakened and vortex shedding was suppressed. Prothin et al.[23] applied the POD method to highlight the 3-D effects due to the re-entrant jet instability or shock wave propagation. Yin et al.[24] used the POD method to study unsteady cavitating flow around a symmetrically twisted hydrofoil. They found that the first mode could capture the large-scale coherent structures during the cavity shedding. Similarly, Liu et al.[25] employed the POD method to analyze the cavitating turbulence fields of the rigid and flexible hydrofoils. They revealed the cavity and vortex structure corresponding to the modes occupying different energy. The POD method optimally reconstructs flow field dataset based on the energy content of the modes, which has great advantages in the extraction and analysis of higher energetic turbulent structures. Therefore, this method is adopted to investigate the dominant structures in cavitating flows in this study.

1. Mathematical formulations and numerical methods

In this study, the homogeneous flow model was used. The vapor phase and the liquid phase are uniformly mixed and there is no speed slip between the two phases. The basic governing equations include mass conservation equation and momentum conservation equation:

$$\frac{\partial \rho}{\partial t}+\frac{\partial(\rho u_j)}{\partial x_j}=0 \tag{1}$$

$$\frac{\partial(\rho u_i)}{\partial t}+\frac{\partial(\rho u_i u_j)}{\partial x_j}=-\frac{\partial p}{\partial x_i}+\frac{\partial}{\partial x_j}\left(\mu\frac{\partial u_i}{\partial x_j}\right) \tag{2}$$

where ρ, p and μ are the mixture density, mixture pressure and viscosity, u_i and u_j represent the flow velocity of the fluid in the i and j directions respectively. The density ρ and viscosity μ are defined as:

$$\rho=\alpha_v\rho_v+(1-\alpha_v)\rho_l \tag{3}$$

$$\mu=\alpha_v\mu_v+(1-\alpha_v)\mu_l \tag{4}$$

where α_v is the vapor volume fraction, subscripts v and l represent vapor phase and liquid phase, respectively.

1.1 *Turbulence model*

The PANS turbulence model based on the

standard k-ε model is used in this study. The form of the model control equation is the same as that of the standard k-ε, but the dissipation coefficient is modified. The control equations are as follows:

$$\frac{\partial(\rho k_u)}{\partial t}+\frac{\partial}{\partial x_j}(\rho u_j k_u)=\frac{\partial}{\partial x_j}\left[\left(\mu+\frac{\mu_u}{\sigma_{ku}}\right)\frac{\partial k_u}{\partial x_j}\right]+P_u-\rho\varepsilon_u \tag{5}$$

$$\frac{\partial(\rho\varepsilon_u)}{\partial t}+\frac{\partial}{\partial x_j}(\rho u_j \varepsilon_u)=\frac{\partial}{\partial x_j}\left[\left(\mu+\frac{\mu_u}{\sigma_{\varepsilon u}}\right)\frac{\partial \varepsilon_u}{\partial x_j}\right]+$$

$$\frac{\varepsilon_u}{k_u}(C_{\varepsilon 1}P_u-C^*_{\varepsilon 2}\rho\varepsilon_u) \tag{6}$$

where μ_u, $C^*_{\varepsilon 2}$ are given by

$$\mu_u=C_\mu\rho\frac{k_u^2}{\varepsilon_u} \tag{7}$$

$$C^*_{\varepsilon 2}=C_{\varepsilon 1}+\frac{f_k}{f_\varepsilon}(C_{\varepsilon 2}-C_{\varepsilon 1}) \tag{8}$$

where $C_\mu=0.09$, $C_{\varepsilon 1}=1.44$ and $C_{\varepsilon 1}=1.92$, the other modified coefficients are as follows:

$$\sigma_{ku}=\sigma_k\frac{f_k^2}{f_\varepsilon},\quad \sigma_{\varepsilon u}=\sigma_\varepsilon\frac{f_k^2}{f_\varepsilon} \tag{9}$$

where $\sigma_k=1.0$, $\sigma_\varepsilon=1.3$, the control parameter f_k refers to the ratio of unresolved turbulent kinetic energy to total turbulent kinetic energy and f_ε refers to the ratio of unresolved dissipation to total dissipation, respectively defined as

$$f_k=\frac{k_u}{k},\quad f_\varepsilon=\frac{\varepsilon_u}{\varepsilon} \tag{10}$$

The subscript u represents the physical quantity of the PANS model, $f_k=1$ means that the turbulence equation is restored to the standard k-ε model, $f_k=0$ means that no turbulence model is introduced and it is the solution method of DNS. The value of f_k in this study is 0.2.

1.2 *Cavitation model*

The Zwart cavitation model based on the simplified Rayleigh-Plesset equation is used to simulate the cavitation process. The model assumes that there are spherical bubbles in the liquid region, there is no interaction between the bubbles, and all the bubbles are the same size. The mass transfer equation is given by

$$\frac{\partial(\rho_v\alpha_v)}{\partial t}+\frac{\partial(\rho_v\alpha_v u_j)}{\partial x_j}=\dot{m}^+-\dot{m}^- \tag{11}$$

where $\dot{m}^+$ and $\dot{m}^-$ represent the evaporation source term and the condensation source term, respectively defined as

$$\dot{m}^+=F_{\text{vap}}\frac{3\alpha_{\text{nuc}}(1-\alpha_v)\rho_v}{R_B}\sqrt{\frac{2(p_v-p)}{3\rho_l}},\quad p\le p_v \tag{12}$$

$$\dot{m}^-=F_{\text{cond}}\frac{3\alpha_v\rho_v}{R_B}\sqrt{\frac{2(p-p_v)}{3\rho_l}},\quad p>p_v \tag{13}$$

where F_{vap} and F_{cond} are the coefficients for the vaporization and condensation processes with the values of 50 and 0.01, α_v is the vapor volume fraction, the nucleation site volume fraction $\alpha_{\text{nuc}}=5\times10^{-4}$ and the value of bubble radius is $R_B=10^{-6}$ m.

1.3 *Control of cavitation with WCG*

When the fluid on the surface of the hydrofoil cannot overcome the adverse pressure gradient due to the effect of viscosity, flow separation will occur. It is one of the important causes of cavitation. The laminar separation bubble (LSB) is the recirculation region between the boundary layer separation point and the reattachment point. One of the main reasons for its formation is Tollmien-Schlichting instability. Figure 1(a) shows the schematic of boundary-layer separation point, laminar bubble separation region, and reattachment point of the suction surface when the benchmark hydrofoil has no cavitation. Kadivar et al.[17] found that the WCG inserted behind the reattachment point could increase the local pressure, suppress laminar separation bubble and the cavitation inception, leading to cavity occurred downstream of the WCG, as shown in Fig. 1(b). As mentioned in the introduction, the formation characteristics of cavitation are closely related to laminar flow separation. Actually, due to the existence of cavitating vortices downstream of the WCG, the WCG located upstream of the separation point also plays a vital role in the laminar separation bubble as well as the inception of attached cavitation. In the present study, we try to insert a miniature WCG upstream of the boundary layer separation point to study its influence on cavitation, as shown in Fig. 1(a). Figure 1(b) shows the parameters of the WCG, where

c, x, a and b represent the length of the hydrofoil chord, the distance of WCG from the leading edge and the length and height of WCG, respectively.

1.4 *Boundary conditions and numerical setup*

The research object of this paper is the NACA66 benchmark hydrofoil with an angle of attack of 8°. The chord length of the hydrofoil is $c = 0.1$ m and the span length is $s = 0.15$ m. Due to the symmetry of the hydrofoil, only half of the space was taken as the computational domain. Numerical simulations were performed in the domain of length, width and height of $9c$, $0.75c$ and $2.5c$, respectively. The boundaries of the computational domain were set to free slip and the hydrofoil surface was non-slip, as shown in Fig. 2. The time step of numerical calculation was set to 2×10^{-4} s.

The water at 25°C and water vapor at the same temperature were selected as fluid medium for numerical calculation, and the saturated vapor pressure is $p_v = 3169$ Pa. The constant inlet velocity and outlet pressure were given as $U = 10$ m/s, $p = 78\,019$ Pa, respectively, which results in the cavitation number $\sigma = 1.5$. The right region of Fig. 2 shows the grid distribution around the two hydrofoils surfaces. The computational domain adopts a hexahedral structured grid, and the grid refinement is performed on the near-wall region of the hydrofoil.

1.5 *Numerical calculation method verification*

The cloud cavitation evolution during one typical oscillation cycle for the benchmark hydrofoil under experiment[26] and numerical simulation is shown in Fig. 3. Cavitating flows were simulated based on the commercial software ANSYS CFX 19.0. The results show that the cavity evolution of numerical simulation agrees well with the experiment. The cavity first occurs on the leading edge of the hydrofoil, as time

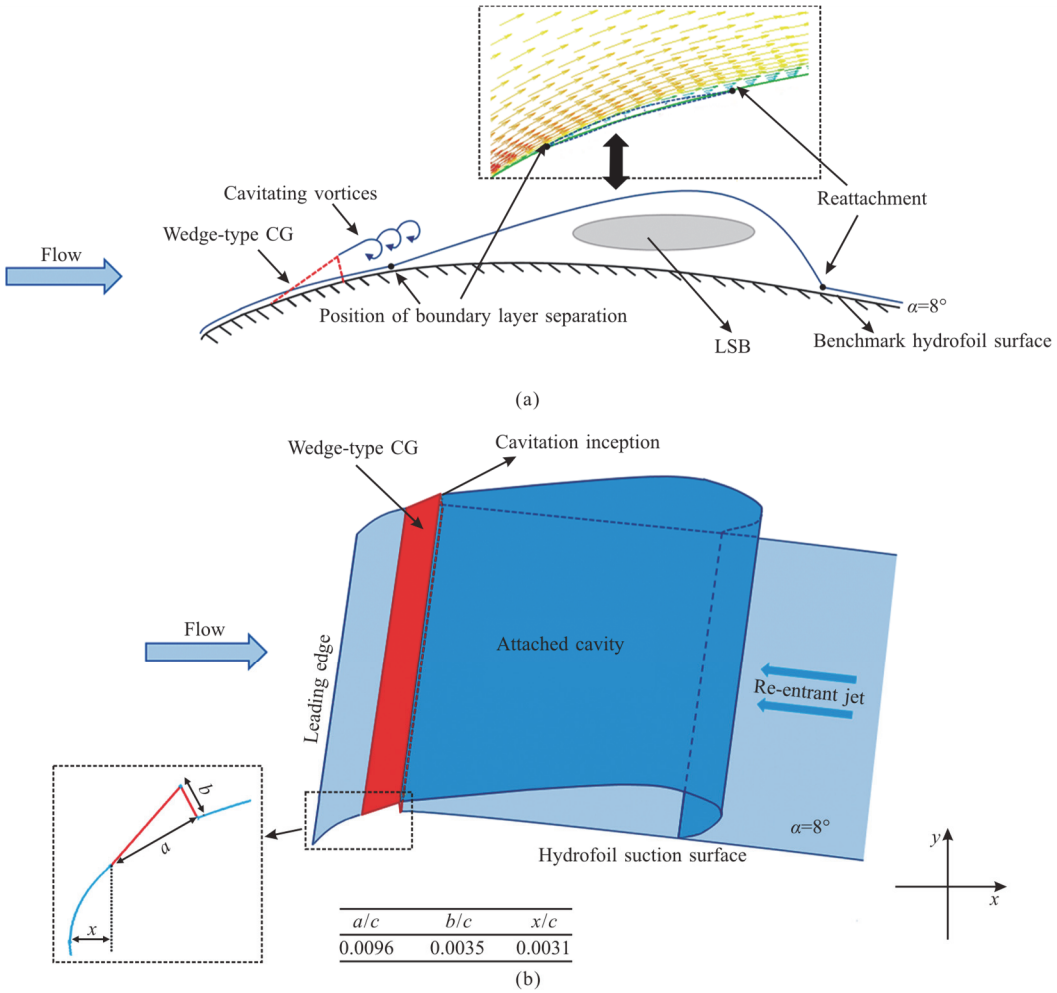

Fig. 1 (Color online) (a) Schematic diagram of boundary layer separation point, laminar bubble separation region, and attachment point of the benchmark hydrofoil suction surface, and the location of WCG, (b) Schematic view of the position of cavitation inception for the hydrofoil with WCG, the size of WCG and the development direction of re-entrant jet of the hydrofoil suction surface. The symbols c, x, a and b represent the length of the hydrofoil chord, the distance of WCG from the leading edge and the length and height of WCG, respectively

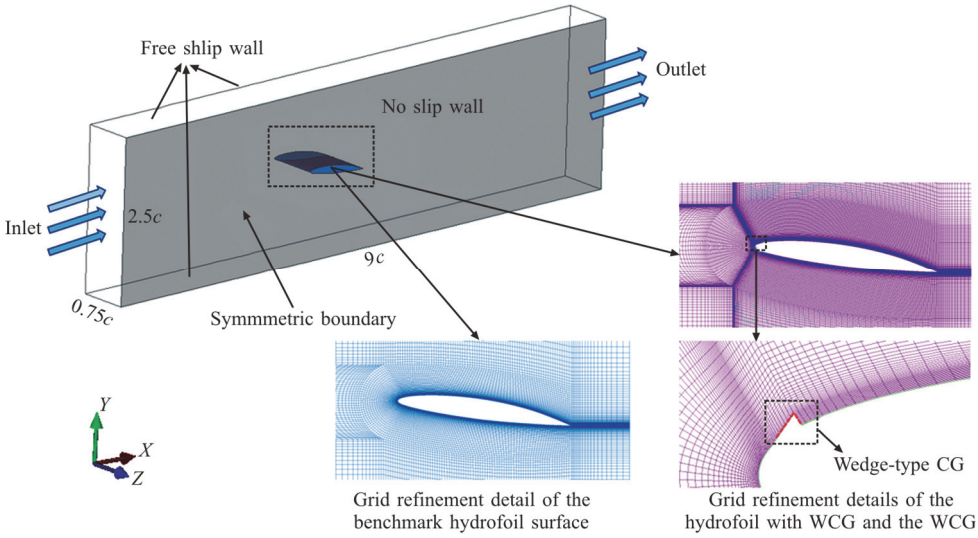

Fig. 2 (Color online) The computational domain, boundary conditions and grid refinement

Table 1 The time-average value of the drag coefficients of the hydrofoil without WCG and with WCG under different meshes

Mesh size	Nodes		C_D	
	Without WCG	With WCG	Without WCG	With WCG
Coarse	261 126	1 732 275	0.094	0.131
Mid-size 1	580 280	3 118 095	0.089	0.123
Mid-size 2	870 420	4 157 460	0.090	0.122
Fine	1 160 560	5 196 825	0.089	0.122

goes by, the cavity gradually develops downstream. When the cavity develops to a certain length, the cavity breaks in the spanwise direction, and then shedding and collapse of the cavitation clouds appear.

Table 1 shows the time-average value of the drag coefficients of benchmark hydrofoil and the hydrofoil with WCG under different meshes. It can be seen from the figure that after the third set of mesh, with the increase of nodes, the drag coefficient hardly increases. Therefore, to balance computing applicability and efficiency, the Mid-size 2 was selected in this paper.

2. Proper orthogonal decomposition

POD is a kind of optimization technology in the sense of energy, because it only needs a few characteristic functions to restore the flow dynamics. In this study, the spatial nodes are dense. In order to improve computational efficiency, the snapshot POD method proposed by Sirovich[27] is chosen. Its basic idea is to solve the correlation matrix C of the matrix U containing N time steps for the flow field, and then find out the first r modes which represent the main characteristics of the flow field. The specific solution is as follows:

All velocity components from the N snapshots are arranged in a matrix U as

$$U=[u^1\ u^2\cdots u^N]=\begin{bmatrix} u_1^1 & u_1^2 & \cdots & u_1^N \\ u_2^1 & u_2^2 & \cdots & u_2^N \\ \vdots & \vdots & \vdots & \vdots \\ u_M^1 & u_M^2 & \cdots & u_M^N \end{bmatrix} \tag{14}$$

Time correlation matrix C of matrix U is

$$C=\frac{1}{N}U^{\mathrm{T}}U \tag{15}$$

Solve the eigenvalues λ_i and eigenvectors A^i of the matrix C

$$CA^i=\lambda_i A^i \tag{16}$$

The eigenvector of matrix C determines the construction of the POD mode, and the eigenvalue represents the energy of the corresponding mode. Large eigenvalues correspond to POD modes with higher weights, hence only a few high-energy modes need to be retained to effectively capture the main characteristics of the original flow field. Usually, the solutions are arranged in descending order according to the size of eigenvalues, namely

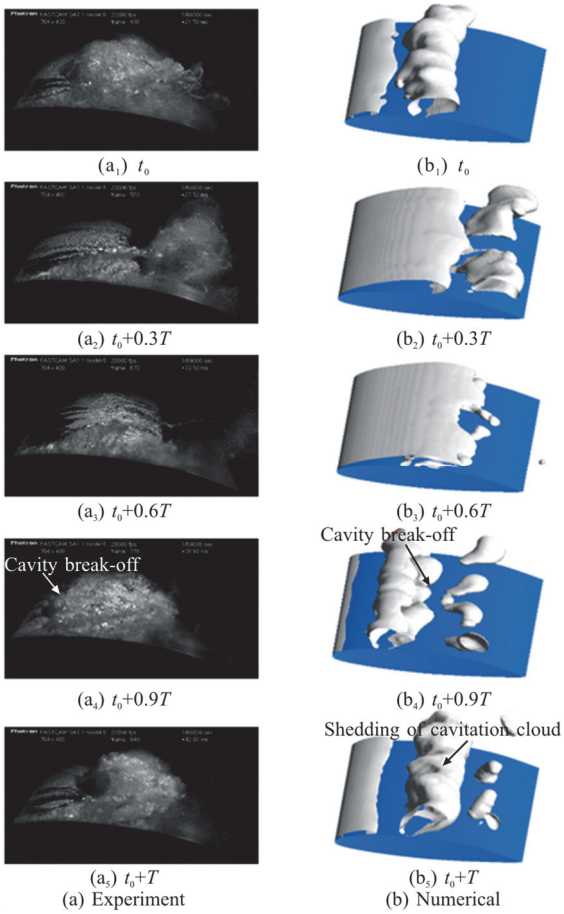

Fig. 3 (Color online) Instantaneous photographs of the unsteady cloud cavitation evolution during one typical oscillation cycle for the benchmark hydrofoil under experiment[26] and numerical simulation

$$\lambda_i > \lambda_{i+1}, \quad \lambda_1 > \lambda_2 > \cdots > \lambda_N = 0 \tag{17}$$

The POD modes ϕ^i are then given by

$$\phi^i = \frac{\sum_{n=1}^{N} A_n^i u^n}{\left\| \sum_{n=1}^{N} A_n^i u^n \right\|} \tag{18}$$

where A_n^i is the n^{th} component of the eigenvector corresponding to the i^{th} eigenvalue, N is the number of snapshots and $\|\cdot\|$ represents the 2-norm on the inner product space.

By projecting the velocity field to the POD modes, the modal coefficients (also called POD coefficients or time varying coefficients) are obtained

$$a_n = \varphi^{\mathrm{T}} U \tag{19}$$

where $\varphi = [\phi^1\ \phi^2 \cdots \phi^N]$ is the modal matrix of each order.

Then, the flow field of the n^{th} snapshot can be reconstructed from the modal decomposition

$$u^n = \sum_{i=1}^{N} a_n^i \phi^i = \varphi a_n \tag{20}$$

The measured flow field is regarded as composed of several main structures, and these structures are displayed in order of energy level by the POD method, so as to find out the flow field that plays a main control role in the flow field. In this study, POD is used to study cavity dynamics by modal decomposition of flow field snapshot data.

3. Results and discussion

Figure 4 shows the vapor volume fraction iso-surface and the Q-criterion iso-surface for the cloud cavitation during one oscillation cycle for the hydrofoil without and with WCG. The Q-criterion defines the second invariant of the velocity gradient tensor. When $Q > 0$, it indicates that the rotation effect is dominant, and when $Q < 0$, the shear effect is dominant. Q-criterion is one of the effective methods to visualize the vortex structure of the flow field[28], whose expression can be given by

$$Q = \frac{1}{2}\left[\left(\frac{\partial u_i}{\partial x_i}\right)^2 - \frac{\partial u_i}{\partial x_j}\frac{\partial u_j}{\partial x_i}\right] \tag{21}$$

As shown in Fig. 4, the periodic process of cavity formation, growth, break-off, shedding and collapse during cavity evolution can be observed for the two hydrofoils. The cavity forms on the hydrofoil suction surface at t_0 and develops downstream with the cavitation cloud shedding of the previous cycle. At about $t_0 + 0.6T$, the length of the attached cavity reaches the maximum, and then the cavity breaks due to the re-entrant jet[29], as shown at $t_0 + 0.9T$. Finally, these broken cavities merge again to form the cavitation cloud, which sheds and collapses downstream, as shown at $t_0 + T$.

Compared with the hydrofoil without WCG, the hydrofoil with WCG shows some differences during cavity evolution. First of all, the cavity of the hydrofoil with WCG forms behind the WCG and appears as irregular lines of different sizes, while the cavity of the hydrofoil without WCG covers the hydrofoil leading edge in a sheet shape and develops smoothly downstream, as shown in Fig. 5. This is because using

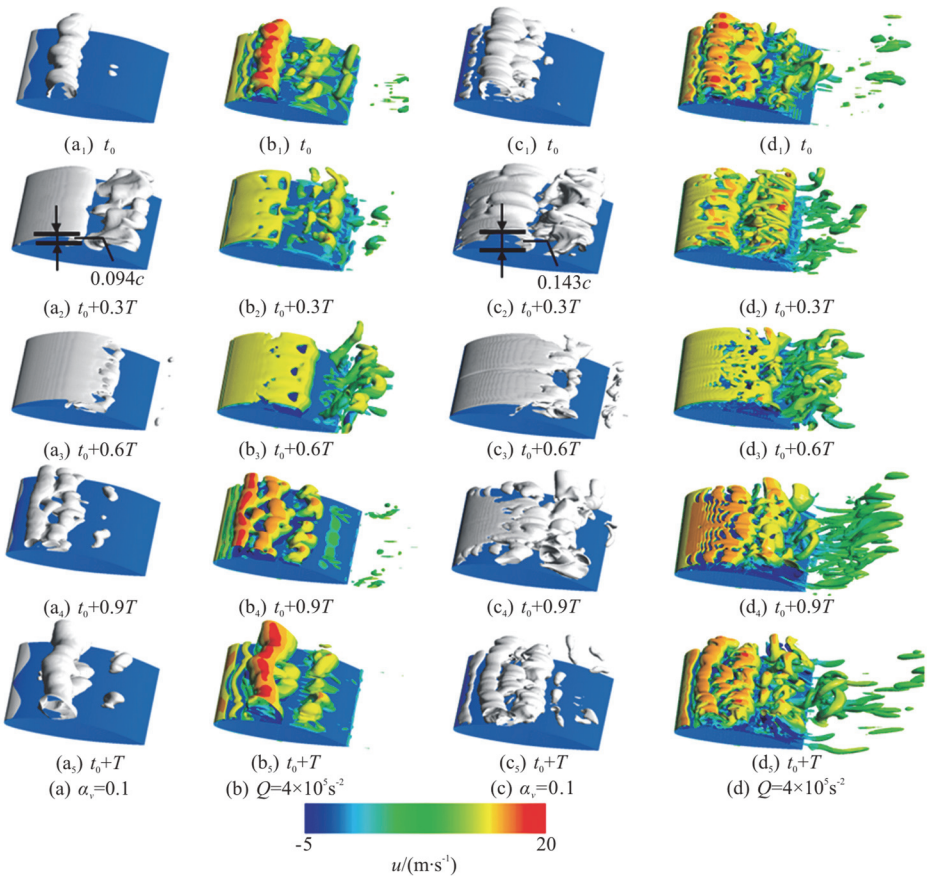

Fig. 4 (Color online) Vapor volume fraction iso-surface ($\alpha_v = 0.1$) and the Q-criterion iso-surface ($Q = 4\times10^5\,\mathrm{s}^{-2}$, colored by streamwise velocity) for the cloud cavitation during one oscillation cycle for the hydrofoil without and with WCG

WCG significantly increases the pressure behind WCG and moves the lowest pressure region downstream, then alters the initial position of the attached cavity, as shown in Fig. 6. The pressure coefficient C_p is calculated by the equation $C_p = (p - p_\infty)/(0.5\rho_l U^2)$, where p, p_∞ and ρ_l are the local pressure, reference pressure and the density of the fluid, respectively. In addition, the perturbation of cavitating vortices behind WCG on flow field resulted in the cavity for the hydrofoil with WCG shows a more irregular and chaotic state during cavity evolution, accompanied by more shedding of small-scale cavity structures, as shown at $t_0 + 0.9T$, $t_0 + T$. Thus, more abundant small-scale vortex structures can be seen from the Q-criterion iso-surface in Fig. 4. Moreover, it is found that WCG can increase the thickness of the attached cavity (the thickness for the hydrofoil without WCG is about $0.094c$, and for the hydrofoil with WCG is about $0.143c$), resulting in an attached cavity of larger scale for the hydrofoil with WCG.

The time history of lift and drag coefficients fluctuations for the two hydrofoils under cloud cavitation is shown in Fig. 7. The time-average lift coefficient for the hydrofoil with WCG is higher than that for the hydrofoil without WCG. However, due to the time-average drag coefficient increased significantly after using WCG, the time-average lift to drag ratio for the hydrofoil with WCG is slightly lower than that for the hydrofoil without WCG, which are $C_l / C_d = 9.26$, 11.93, respectively. This result is consistent with the conclusion of Kadivar et al.[15]. In addition, from the FFT results of time history of drag coefficient in Fig. 8, it can be seen that the dominant frequency for the hydrofoil with WCG is obtained at $St = fc/U = 0.475$, while for the hydrofoil without WCG it is obtained at $St = 0.525$, which indicates that the characteristic frequency of the cavity evolution for the hydrofoil with WCG is lower.

POD is a powerful tool for identifying spatial and temporal coherent structures in a flow. In order to further analyze the characteristics of the cavitation flow field for the two types of hydrofoils, the snapshot velocity field data of the domain around hydrofoils were extracted, as shown in Fig. 9, and the POD method was used for modal decomposition.

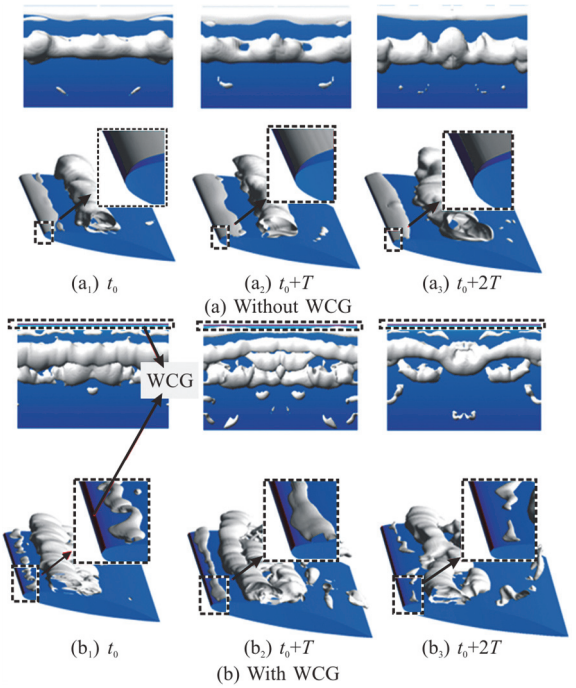

Fig. 5 (Color online) Vapor volume fraction iso-surface ($\alpha_v = 0.1$) at three cavitation inception moments ($\sigma = 1.5$) on the hydrofoil suction surface

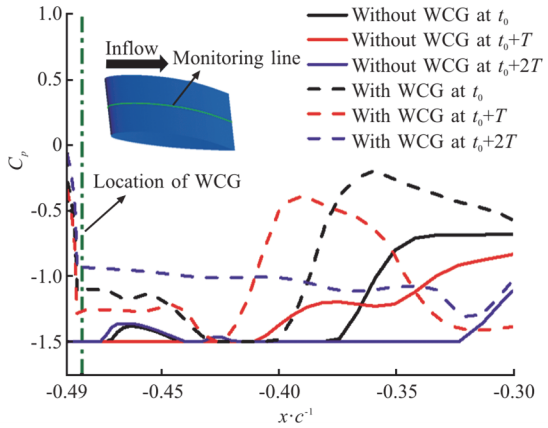

Fig. 6 (Color online) Instantaneous pressure coefficient on the monitoring line of the hydrofoil suction surface

For the accuracy of POD mode analysis, the first step is to check the convergence in the domain, and the calculation of POD convergence can determine the number of snapshots needed for validating the decomposition. That is, by using different time intervals to calculate the energy of the low-order mode under different snapshot numbers, if the energy of the mode does not change significantly with the increase in the number of snapshots, this would indicate that the modes have converged. In other words, adding more snapshots does not provide additional information. Figure 10 shows the contribution of the modes $j(j = 0\text{-}3)$ in the reconstruction of instantaneous images calculated as $\lambda_j / \sum_{j=0}^{N} \lambda_j$. It can be seen from the figure that with the increase of the number of snapshots, the energy change amplitude of each mode decreases, and tends to be constant when it reaches 500. This analysis shows that 500 snapshots are sufficient to obtain accurate results.

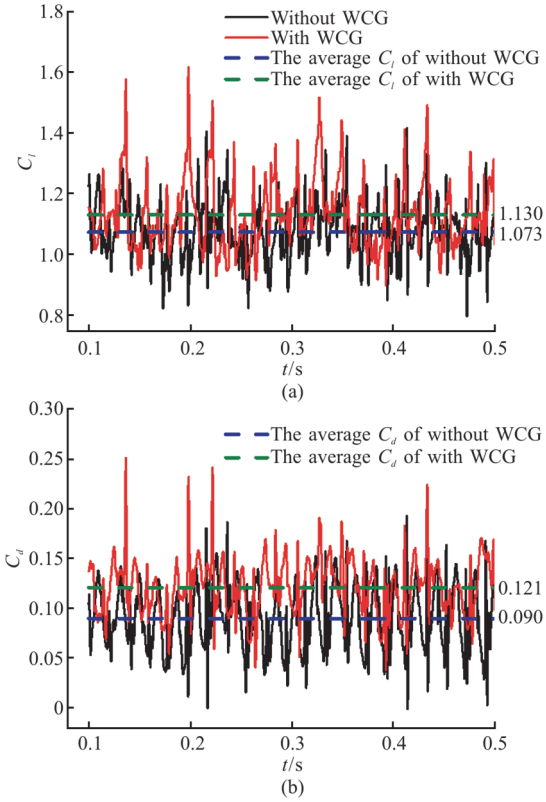

Fig. 7 (Color online) Time history of lift and drag coefficients

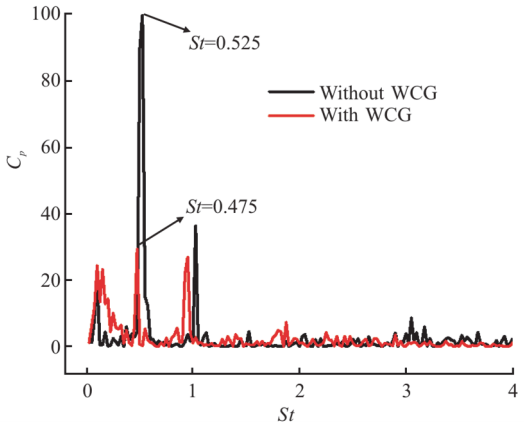

Fig. 8 (Color online) Instantaneous pressure coefficient on the monitoring line of the hydrofoil suction surface

The mode 0 of POD represents the mean flow in

which the flow structure neither increases nor decays with time, and the comparison of time-averaged original flow fields and mean flow represented by mode 0 for the two hydrofoils is shown in Figs. 11(a), 11(b) respectively. It can be seen that the mean flow profile captured by POD is very similar to the time-averaged original flow field, indicating that the number of snapshots is sufficient for the analysis, this is a simple verification of the stationarity and accuracy of the statistical data[30].

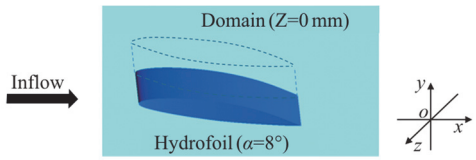

Fig. 9 (Color online) The POD data processing domain

Since the value of eigenvalues corresponds to the weight of POD modes, if they are arranged in descending order, the energy contribution rate of the modes with lower order to the original flow field is greater, that is, they correspond to the structure with higher energy. POD eigenvalues and cumulative contributions according to energy order are shown in Fig. 12. It can be seen that the first five modes (modes 0-4) for the two hydrofoils contribute about 94.99%, 94.51% (more than 90%) of the flow field energy, and the energy contribution of mode 4 occupies about 0.9%, 0.73% (less than 1%) respectively. Therefore, the first 5 modes are retained to reconstruct the original flow field, and the remaining modes with lower energy are filtered out in this paper.

The main modes of POD can reveal the spatial structures of higher energy in the flow field. Therefore, the main characteristics of cavity evolution can be obtained by analyzing the structure distribution of the main POD modes. Figure 13 shows the dominant POD modes (modes 1-4), where mode 1 represents the flow structure with maximum energy on the surface of the two hydrofoils. For the hydrofoil without WCG, mode 1 represents the large-scale cavitation cloud structure formed by the cavity being cut off at the leading edge of the hydrofoil by the re-entrant jet, while for the hydrofoil with WCG, it represents the large-scale cavity structure that develops downstream. The positive and negative structures of modes 2-4 highlight the small-scale vortex structures with less energy separated from the hydrofoil suction surface, and they reveal the oscillations near the large-scale coherent structure, so as to correct the features of the flow field and obtain the accurate flow field. In addition, it can be found that the regions of positive and negative structures of the hydrofoil with WCG in modes 2-4 are smaller, which highlights the shedding of small-scale cavity structures during cavity evolution. It should be noted that each mode in the POD

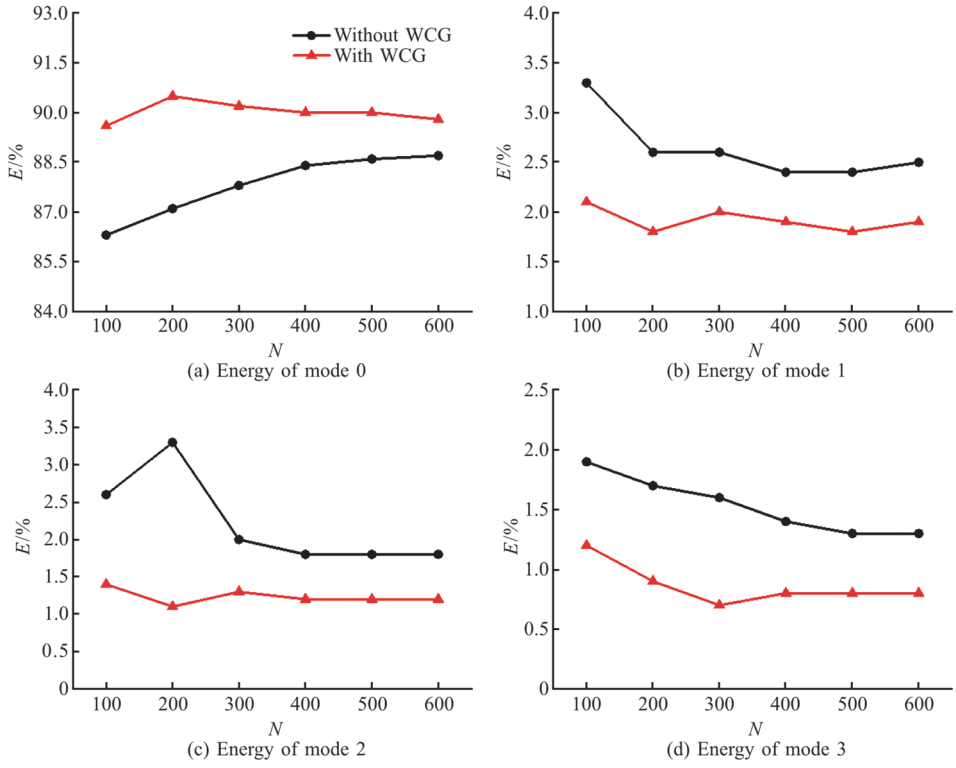

Fig. 10 (Color online) Convergence of the POD calculation with $\sigma = 1.5$, energy of modes according to the number of snapshots used for the POD

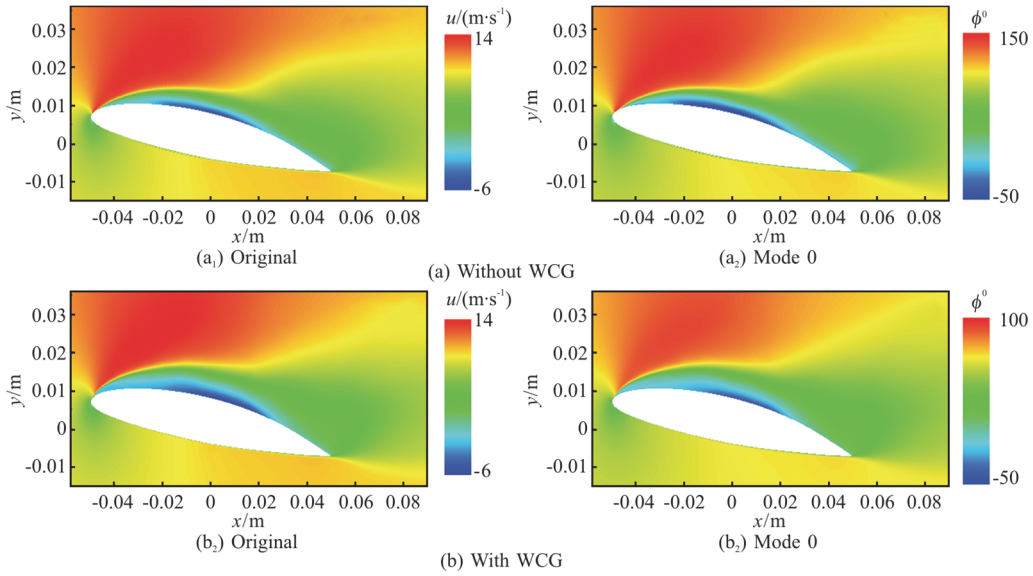

Fig. 11 (Color online) Comparison of time-averaged original flow fields and mean flow represented by mode 0 of POD

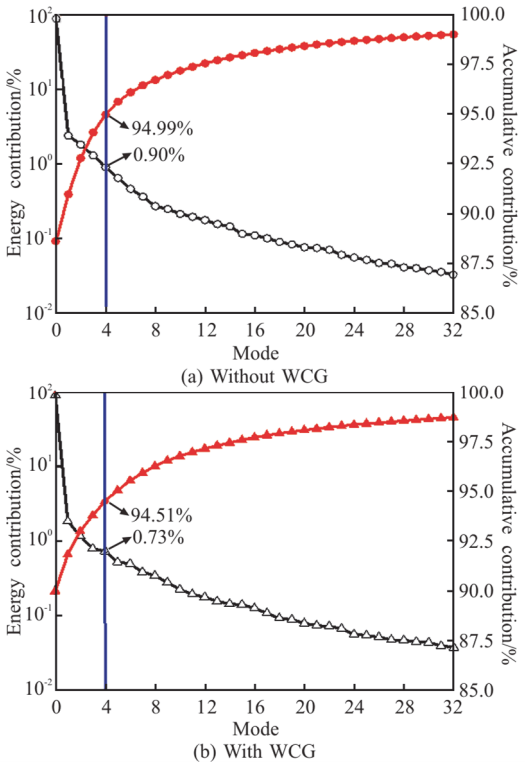

Fig. 12 (Color online) POD eigenvalues and cumulative contributions according to energy order

algorithm contains energy features from multiple flows, thus the POD mode alone cannot reproduce the transient flow field.

The temporal eigenfunctions and their FFT results of the modal coefficients for POD modes 1-4 of the two hydrofoils are shown in Fig. 14. Since the POD modes may contain multiple frequency components, it can be seen from the left of Fig. 14 that the temporal eigenfunctions are not completely simple harmonic waves. In addition, as shown at the right of Fig. 14, the dominant frequencies of the first two modal coefficients of the two hydrofoils are the same, which are $St = 0.500$ $(f = StU / c = 50\ \text{Hz})$, $St = 0.475$ (47.5 Hz) respectively. They are very close to the characteristic frequencies of the cavitation cloud shedding, which are 52.5 Hz, 47.5 Hz respectively. Therefore, the first two modes can characterize the periodic shedding process of cavitation cloud, and the shedding frequency of cavitation cloud for the hydrofoil with WCG is lower than that for the hydrofoil without WCG. At the same time, due to the shedding frequency of the cavitation cloud being dominant in the cavitating field, the amplitude of the dominant frequency usually decreases as the mode increases, matching with the energy attenuation. As for the dominant frequencies of the third and fourth modes, they represent the shedding frequency of cavities or vortices with smaller scale.

The correlation distribution of the modal coefficients a_1, a_2 for the two hydrofoils is shown in Fig. 15. It can be found that the modal coefficients a_1, a_2 oscillate around zero, the distribution radius of these coefficient points is quite different due to the abundant scale of vortex structures around the hydrofoils, and the energy content of these vortex structures is positively correlated with the distribution radius[31]. The modal coefficient points of the hydrofoil without WCG are more concentrated near the zero point, indicating that the vortex structures around the hydrofoil without WCG have less energy and lower turbulence intensity. This is related to the smaller scale

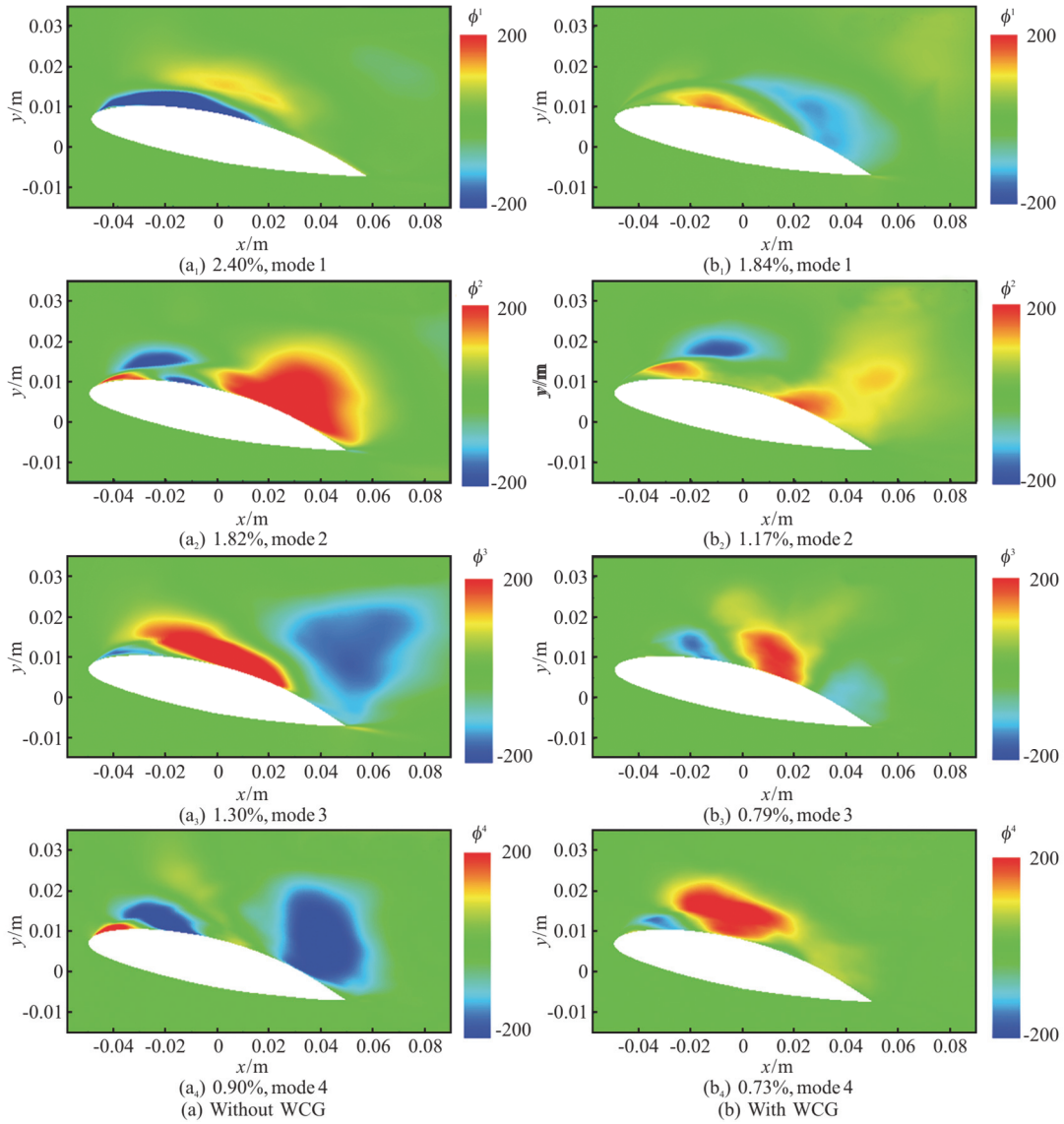

Fig. 13 (Color online) Dominant POD modes (modes 1-4, $\sigma = 1.5$). Percentages represent the contribution of the POD modes to flow field reconstruction

cavities shedding during cavity evolution. On the other hand, whether the distribution of coefficient points is circumferentially related to the circle in the Fig. 15 reflects the periodic strength of the large-scale vortex structures in the flow field. It can be found that the periodicity of the vortex structures for the two hydrofoils is weak, which may be due to the influence of the vortex structures of different scales and the irregular turbulence caused by the cavitation.

The reconstruction of the flow field based on the first 5 POD modes can basically reflect the characteristics of the flow field. The root mean square error (RMSE) of the reconstructed flow field in Fig. 16 shows how well the reconstructed flow matches the original flow field, which can be calculated as given by

$$\mathrm{RMSE} = \sqrt{\frac{1}{m}\sum_{i=1}^{m}(u_i^{\mathrm{actual}} - u_i^{\mathrm{reconstructed}})^2} \tag{22}$$

where m is the number of grid nodes in a given snapshot.

It can be seen from Fig. 16 that the RMSE of the reconstructed flow field for the hydrofoils fluctuates with cavity evolution. However, the time-averaged reconstruction error for the hydrofoil with WCG is higher than that without WCG. This is because the hydrofoil with WCG is accompanied by the shedding of more abundant small-scale vortex structures during the cavity evolution. Therefore, more small-scale structures will be selectively filtered during flow field reconstruction, resulting in higher errors. In addition, from the time-averaged RMSE contour of reconstructed

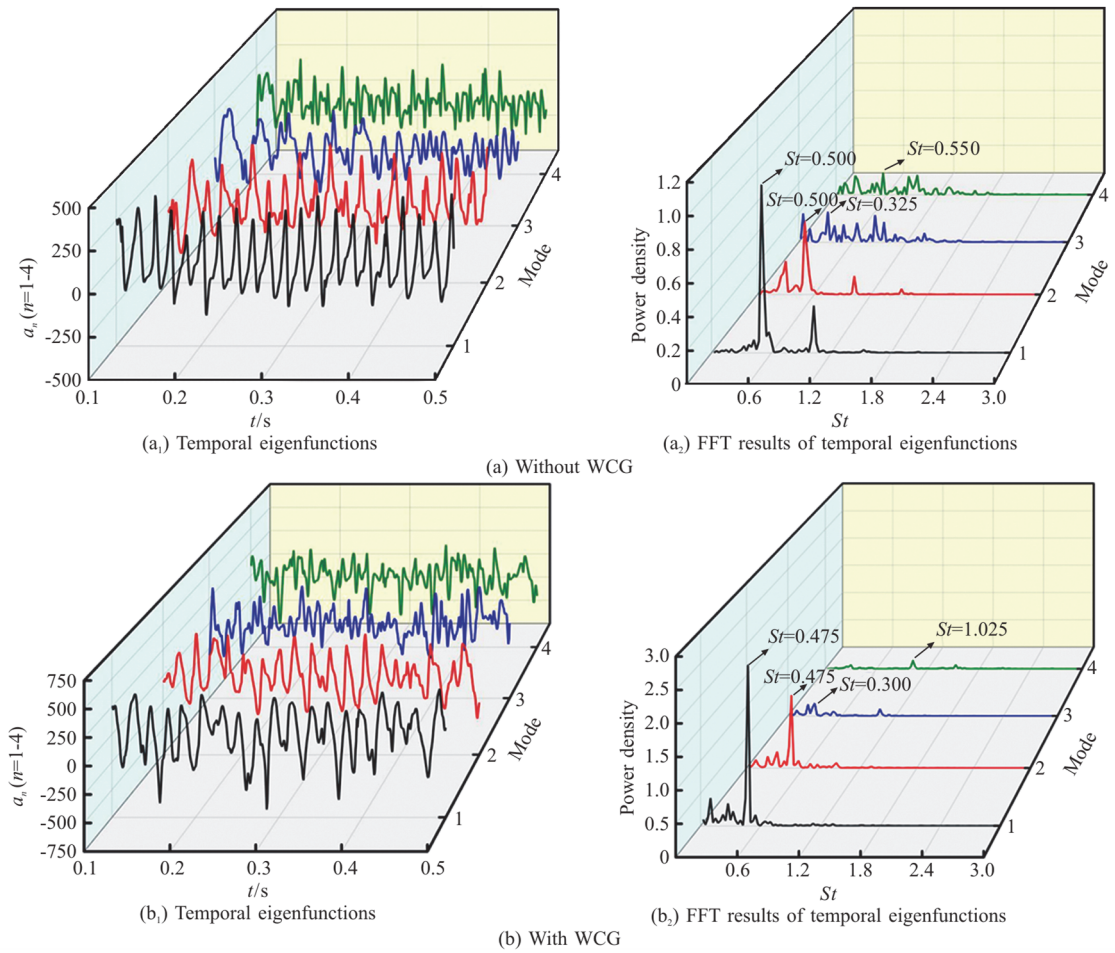

Fig. 14 (Color online) Modal coefficients for POD modes 1-4

flow field in Fig. 17, it can be found that the higher error regions for the two hydrofoils are above the suction surface, especially the vapor-liquid interface region of the cavitation flow field. It is caused by the instability of the vapor-liquid interface which will induce more small-scale vortex structures.

The flow field contains various vortex structures with different scales. Due to the influence of various small-scale vortex structures and turbulent dissipation on the flow, it is difficult to visually observe the spatial distribution characteristics of large-scale coherent structures in the flow field. Therefore, reconstructing the flow field to filter out small-scale structures and background noise is one of the purposes of using the POD method. The flow fields reconstructed by the first 5 modes during one oscillation cycle for the two hydrofoils are shown in Figs. 18, 19, respectively. It is obvious that the boundary between different velocity regions of the reconstructed flow field is clearer and smoother. The re-entrant jet that gradually develops upstream along the hydrofoil suction surface and the high positive velocity region that gradually diffuses from the leading edge to the downstream are captured, which implies the periodic evolution of cavity. However, during the reconstruction for the hydrofoil with WCG, more small-scale structures are filtered, which leads to a larger reconstruction error, as shown in Fig. 16.

4. Conclusions

In this paper, a passive method of cavitating flow control called WCG was investigated. The WCG was installed upstream of the flow separation point on the suction surface of NACA66 hydrofoil. The PANS turbulence model based on standard k-ε and the Zwart cavitation model were used to simulate the unsteady cloud cavitation. Then, the effects of the WCG on cavity evolution, vortex structure and hydrodynamic performance were investigated. In addition, the POD method was adopted to further analyze the characteristics of the cavitation flow field with and without WCG. The results are summarized as follows:

(1) The WCG can increase the thickness of the attached cavity, alter the attached cavity to be with a rough surface and cause the cavity inception behind

the WCG instead of the leading edge. For the hydrofoil with WCG, there is a larger-scale attached cavity accompanied with more shedding behaviors of cavities with small scales, which probably explains why it can decrease the dominant frequency of the unsteady cavitation evolution.

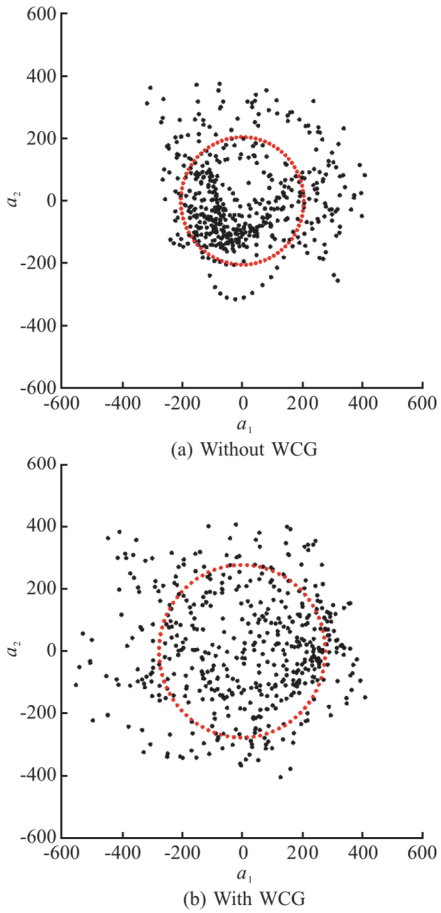

Fig. 15 (Color online) The correlation distribution of POD modal coefficients for modes 1, 2. The radius R of the circle is obtained by the calculation formula $\langle a_1^2 \rangle + \langle a_2^2 \rangle = R^2$, $\langle \cdot \rangle$ is the average operator

(2) The POD method can extract the dominant flow structures, identify the energy content of the vortex structures, and obtain the reconstructed flow field with the main characteristics. The frequency obtained by the analysis of the first two POD modal coefficients can represent the dominant frequency of cloud shedding behaviors. The hydrofoil with WCG has more small-scale vortex structures during the cavity evolution, resulting in a larger reconstruction error. The correlation distribution of POD modal coefficients shows that the vortex structures around the hydrofoil without WCG have less energy and lower turbulence intensity.

It should be noted that the present study only discussed the WCG with fixed size and location, and found these interesting conclusions. More experimental and numerical investigations are required to analyze the effects of WCG with different sizes or locations on the formation and development of cavity in future researches.

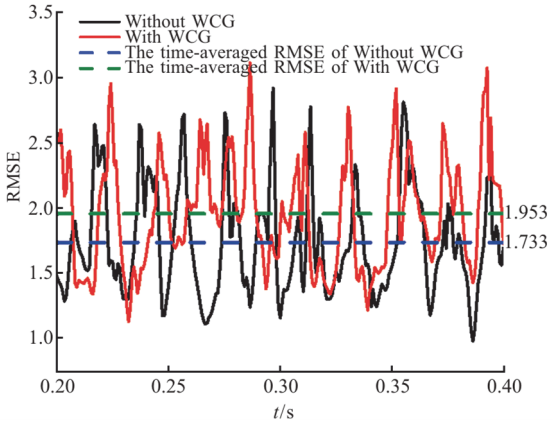

Fig. 16 (Color online) RMSE of reconstructed flow field with the first 5 POD modes

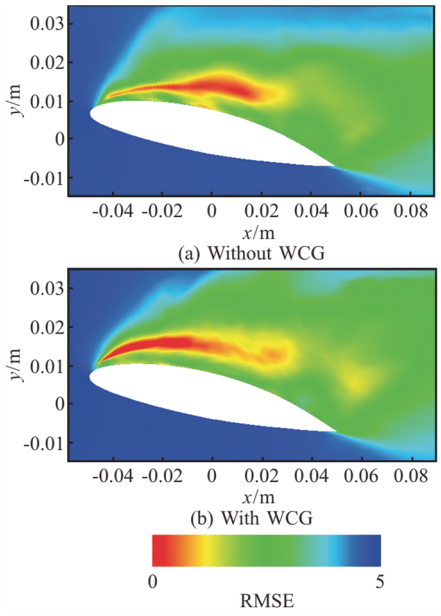

Fig. 17 (Color online) Time-averaged RMSE contour of reconstructed flow field with the first 5 POD modes

Acknowledgment

(This research received other funding agency in the public, commercial, or not-for-profit sectors.)

Compliance with ethical standards

Conflict of interest: The authors declare that they have no conflict of interest.

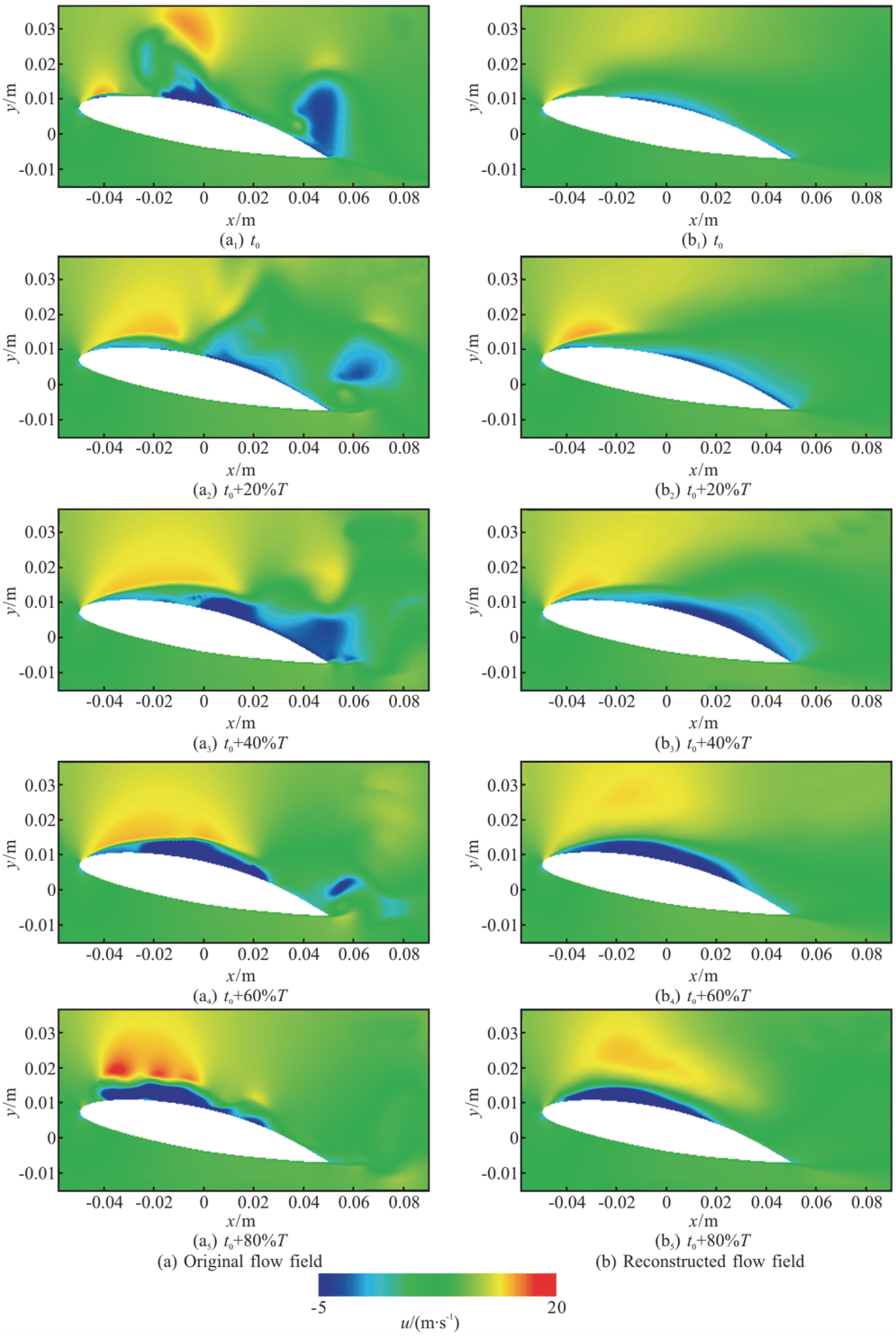

Fig. 18 (Color online) The flow field reconstructed by the first 5 modes during one oscillation cycle for the hydrofoil without WCG

Ethical approval: This article does not contain any studies with human participants or animals performed by any of the authors.

Informed consent: Informed consent was obtained from all individual participants included in the study.

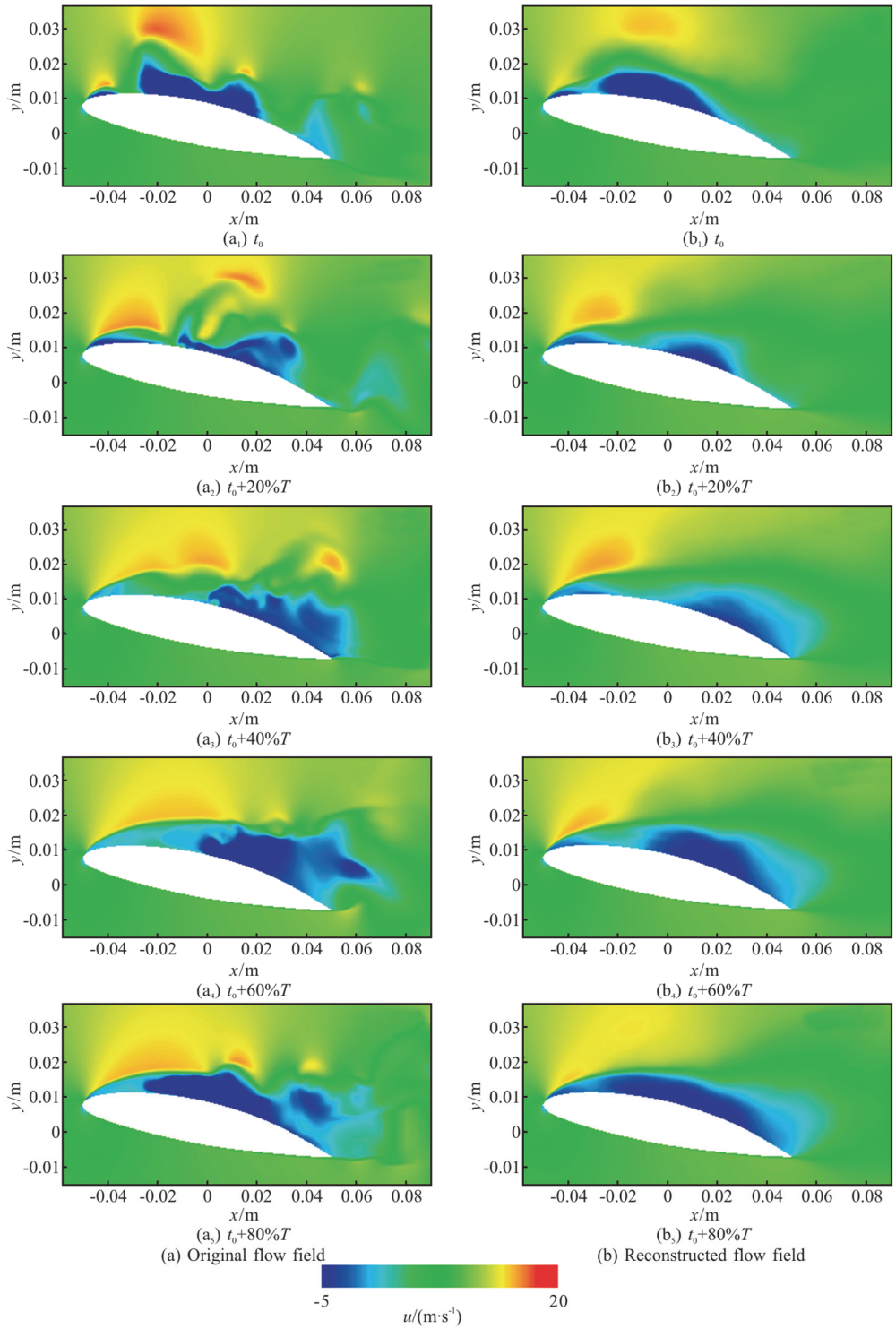

Fig. 19 (Color online) The flow field reconstructed by the first 5 modes during one oscillation cycle for the hydrofoil with WCG

References

[1] Huang B., Qiu S. C., Li X. B. et al. A review of transient flow structure and unsteady mechanism of cavitating flow [J]. *Journal of Hydrodynamics*, 2019, 31(3): 429-444.

[2] Coutier-Delgosha O., Devillers J. F., Leriche M. et al. Effect of wall roughness on the dynamics of unsteady cavitation [J]. *Journal of Fluids Engineering*, 2005, 127(4): 726-733.

[3] Kawanami Y., Kato H., Yamaguchi H. et al. Mechanism and control of cloud cavitation [J]. *Journal of Fluids Engineering*, 1997, 119(4): 788-794.

[4] Zhang L., Chen M., Shao X. Inhibition of cloud cavitation on a flat hydrofoil through the placement of an obstacle [J]. *Ocean Engineering*, 2018, 155: 1-9.
[5] Huang J., Yu C., Wang Y. W. et al. Passive control of cavitating flow around an axisymmetric projectile by using a trip bar [J]. *Theoretical and Applied Mechanics Letters*, 2017, 7(4): 181-184.
[6] Zhao W., Zhao G. An active method to control cavitation in a centrifugal pump by obstacles [J]. *Advances in Mechanical Engineering*, 2017, 9(11): 168781401773294.
[7] Cheng H. Y., Bai X. R., Long X. P. et al. Large eddy simulation of the tip-leakage cavitating flow with an insight on how cavitation influences vorticity and turbulence [J]. *Applied Mathematical Modelling*, 2020, 77: 788-809.
[8] Cheng H., Long X., Ji B. et al. Suppressing tip-leakage vortex cavitation by overhanging grooves [J]. *Experiments in Fluids*, 2020, 61(7): 1-18.
[9] Cheng H. Y., Ji B., Long X. P. et al. A review of cavitation in tip-leakage flow and its control [J]. *Journal of Hydrodynamics*, 2021, 33(2): 226-242.
[10] Lu F., Huang H. B., Zhang Z. R. et al. Application of the vortex generator to control the PHV cavitation [J]. *Journal of Ship Mechanics*, 2009, 13(6): 873-879.
[11] Che B., Chu N., Cao L. et al. Control effect of micro vortex generators on attached cavitation instability [J]. *Physics of Fluids*, 2019, 31(6): 064102.
[12] Che B., Chu N., Schmidt S. J. et al. Control effect of micro vortex generators on leading edge of attached cavitation [J]. *Physics of Fluids*, 2019, 31(4): 044102.
[13] Kadivar E., el Moctar O., Javadi K. Stabilization of cloud cavitation instabilities using cylindrical cavitating-bubble generators (CCGs) [J]. *International Journal of Multiphase Flow*, 2019, 115: 108-125.
[14] Kadivar E., Timoshevskiy M. V., Pervunin K. S. et al. Cavitation control using cylindrical cavitating-bubble generators (CCGs): Experiments on a benchmark CAV2003 hydrofoil [J]. *International Journal of Multiphase Flow*, 2020, 125: 103186.
[15] Kadivar E., Ochiai T., Iga Y. et al. An experimental investigation of transient cavitation control on a hydrofoil using hemispherical vortex generators [J]. *Journal of Hydrodynamics*, 2021, 33(6): 1139-1147.
[16] Kadivar E., el Moctar O., Javadi K. Investigation of the effect of cavitation passive control on the dynamics of unsteady cloud cavitation [J]. *Applied Mathematical Modelling*, 2018, 64: 333-356.
[17] Kadivar E., Timoshevskiy M. V., Nichik M. Y. et al. Control of unsteady partial cavitation and cloud cavitation in marine engineering and hydraulic systems [J]. *Physics of Fluids*, 2020, 32(5): 052108.
[18] Javadi K., Dorostkar M. M., Katal A. Cavitation passive control on immersed bodies [J]. *Journal of Marine Science and Application*, 2017, 16(1): 33-41.
[19] Franc J. P., Michel J. M. Attached cavitation and the boundary layer: Experimental investigation and numerical treatment [J]. *Journal of Fluid Mechanics*, 1985, 154: 63-90.
[20] Croci K., Ravelet F., Danlos A. et al. Attached cavitation in laminar separations within a transition to unsteadiness [J]. *Physics of Fluids*, 2019, 31(6): 063605.
[21] Danlos A., Ravelet F., Coutier-Delgosha O. et al. Cavitation regime detection through proper orthogonal decomposition: dynamics analysis of the sheet cavity on a grooved convergent-divergent nozzle [J]. *International Journal of Heat and Fluid Flow*, 2014, 47: 9-20.
[22] Wang Z., Zhang M., Kong D. et al. The influence of ventilated cavitation on vortex shedding behind a bluff body [J]. *Experimental Thermal and Fluid Science*, 2018, 98: 181-194.
[23] Prothin S., Billard J. Y., Djeridi H. Image processing using proper orthogonal and dynamic mode decompositions for the study of cavitation developing on a NACA0015 foil [J]. *Experiments in Fluids*, 2016, 57(10): 157-182.
[24] Yin T., Pavesi G., Pei J. et al. Numerical investigation of unsteady cavitation around a twisted hydrofoil [J]. *International Journal of Multiphase Flow*, 2021, 135: 103506.
[25] Liu Y., Wu Q., Huang B. et al. Decomposition of unsteady sheet/cloud cavitation dynamics in fluid-structure interaction via POD and DMD methods [J]. *International Journal of Multiphase Flow*, 2021, 142: 103690.
[26] Wu Q. Physical and Numerical investigation of cavitating flow-induced vibrations [D]. Doctoral Thesis, Beijing, China: Beijing Institute of Technology, 2016(in Chinese).
[27] Sirovich L. Turbulence and the dynamics of coherent structures. I. Coherent structures [J]. *Quarterly of Applied Mathematics*, 1987, 45(3): 561-571.
[28] Chen J., Huang B., Wang Y. et al. Numerical investigation of cavitation-vortex interaction with special emphasis on the multistage shedding process [J]. *Applied Mathematical Modelling*, 2021, 96: 111-130.
[29] Wang C., Wang G., Huang B. Dynamics of unsteady compressible cavitating flows associated with the cavity shedding [J]. *Ocean Engineering*, 2020, 209: 107025.
[30] Mohan A. T., Gaitonde D. V., Visbal M. R. Model reduction and analysis of deep dynamic stall on a plunging airfoil [J]. *Computers and Fluids*, 2016, 129: 1-19.
[31] Zhang Q. PIV Measurements of unsteady characteristics of separated and reattaching flow on finite blunt plate- vortex dynamics analysis using proper orthogonal decomposition and dynamic mode decomposition [D]. Doctoral Thesis, Shanghai, China: Shanghai Jiao Tong University, 2015(in Chinese).